NASA/TM–20220005356

Structural Shape Sensing from Strain Data Using the Basis Function Method

Chan-gi Pak
Armstrong Flight Research Center, Edwards, California

June 2022

NASA STI Program Report Series

The NASA STI Program collects, organizes, provides for archiving, and disseminates NASA's STI. The NASA STI program provides access to the NTRS Registered and its public interface, the NASA Technical Reports Server, thus providing one of the largest collections of aeronautical and space science STI in the world. Results are published in both non-NASA channels and by NASA in the NASA STI Report Series, which includes the following report types:

- TECHNICAL PUBLICATION. Reports of completed research or a major significant phase of research that present the results of NASA Programs and include extensive data or theoretical analysis. Includes compilations of significant scientific and technical data and information deemed to be of continuing reference value. NASA counterpart of peer-reviewed formal professional papers but has less stringent limitations on manuscript length and extent of graphic presentations.

- TECHNICAL MEMORANDUM. Scientific and technical findings that are preliminary or of specialized interest, e.g., quick release reports, working papers, and bibliographies that contain minimal annotation. Does not contain extensive analysis.

- CONTRACTOR REPORT. Scientific and technical findings by NASA-sponsored contractors and grantees.

- CONFERENCE PUBLICATION. Collected papers from scientific and technical conferences, symposia, seminars, or other meetings sponsored or co-sponsored by NASA.

- SPECIAL PUBLICATION. Scientific, technical, or historical information from NASA programs, projects, and missions, often concerned with subjects having substantial public interest.

- TECHNICAL TRANSLATION. English-language translations of foreign scientific and technical material pertinent to NASA's mission.

Specialized services also include organizing and publishing research results, distributing specialized research announcements and feeds, providing information desk and personal search support, and enabling data exchange services.

For more information about the NASA STI program, see the following:

- Access the NASA STI program home page at http://www.sti.nasa.gov

- Help desk contact information:

https://www.sti.nasa.gov/sti-contact-form/ and select the "General" help request type.

NASA/TM–20220005356

Structural Shape Sensing from Strain Data Using the Basis Function Method

Chan-gi Pak
Armstrong Flight Research Center, Edwards, California

National Aeronautics and
Space Administration

Armstrong Flight Research Center
Edwards, California, 93523-0273

June 2022

This report is available in electronic form at

http://ntrs.nasa.gov

Abstract

An aircraft shape must be measured during flight to implement an active trim shape control, such as an active dihedral control for a highly flexible aircraft with a high-aspect-ratio wing, and an active sonic boom control for a supersonic transport aircraft. A basis function method for linear as well as geometrically nonlinear structural shape sensing is proposed in this study. Basis functions can be mode shapes, linear static deformation shapes, or geometrically nonlinear static deformation shapes. The proposed basis function method is validated using a high-aspect-ratio wing, a swept test plate, and the National Aeronautics and Space Administration Low Boom Flight Demonstration mission X-59 Quiet Supersonic Technology (QueSST) aircraft (Lockheed Martin, Bethesda, Maryland). A large structural deformation of a high-aspect-ratio wing is successfully captured using the proposed basis function method with less than 0.3-percent prediction error at the wing-tip section. The basis function method gives excellent deformation prediction, even with stress concentration. Performance of the basis functions is compared using the X-59 stabilator sample case. In most of the sample load cases, static deformations give a better correlation with the target deformation than do mode shapes. Wing shape sensing with sparse strain data is also demonstrated in this study using the X-59 QueSST aircraft. Predicted structural deformations match reasonably with the target deformations even without strain gauges on some structural components. The predicted deformations have a good match with the target deformations.

Nomenclature

Acronyms

2D	two-dimensional
3D	three-dimensional
CBAR	simple beam element with two nodes
CBEAM	beam element with two nodes
CHEXA	six-sided solid element with eight nodes
CPENTA	five-sided solid element with six nodes
CQUAD4	quadrilateral plate element with four nodes
CTETRA	four-sided solid element with four nodes
CTRIA3	triangular plate element with three nodes
DOF	degrees of freedom
FE	finite element
FOSS	fiber-optic strain sensing
LE	leading edge
MID	mid-chord
MLG	main landing gear
NASA	National Aeronautics and Space Administration
NLG	nose landing gear
STAB, stab	stabilator
TE	trailing edge
V	vertical

Symbols

N_i	*i*-th nodal weighting factor (or shape function)
nn	number of nodes for an element
$\{q\}$	deformation vector
$\{q_i\}$	nodal deformation
$\{\epsilon_i\}$	nodal strain

$\{\epsilon_s\}$	strain vector at the strain gauge positions
$\{\eta\}$	participation vector
$[\mathbf{T}]$	transformation matrix
$[\mathbf{\Phi}]$	deformation basis function matrix
$\mathbf{\Phi_M}$	deformation basis function matrix corresponds to master degrees of freedom
$\mathbf{\Phi_S}$	deformation basis function matrix corresponds to slave degrees of freedom
$[\mathbf{\Psi_s}]$	strain basis function matrix
$\{\tilde{q}_M\}$	measured master degrees of freedom
$\{q_M\}$	master degrees of freedom
$\{q_S\}$	slave degrees of freedom
α	local angle due to wing taper or dihedral/anhedral effects
β	local sweep angle due to curvilinear sensor line effects
ξ- η	parent coordinates
$\tilde{s}$	distance along the neutral axis direction, in
h	wing thickness
h($\tilde{s}$)	wing thickness at $\tilde{s}$, in
$w(\tilde{s})$	deformation at $\tilde{s}$, in
θ	slope
$\theta(\tilde{s})$	slope at $\tilde{s}$, rad
ϵ_l	axial strain on the lower skin
$\epsilon_l(\tilde{s})$	axial strain at $\tilde{s}$ on the lower skin
ϵ_u	axial strain on the upper skin
$\epsilon_u(\tilde{s})$	axial strain at $\tilde{s}$ on the upper skin
κ	curvature
$\kappa(\tilde{s})$	curvature at $\tilde{s}$, in-1 ($\equiv -(\epsilon_u - \epsilon_l)/h$)
$(*)^T$	transpose of a matrix
$(*)^{-1}$	inverse of a matrix

Introduction

The National Aeronautics and Space Administration (NASA) Helios aircraft (AeroVironment, Arlington, Virginia) experienced a total structural failure 30 min after takeoff from the island of Kauai, Hawaii, on June 26, 2003. Before the mishap, the aircraft faced turbulence and started a divergent pendulum motion in the pitch direction caused by a high center of gravity location and the “persistent” high dihedral configuration (ref. 1). An aeroelastic stability analysis of the aircraft was performed during the mishap investigation. This analysis showed that one of the flexible modes of the aircraft became highly damped at zero frequency, that is, an over-damped response to external loads, before the mishap (p. 41 of reference 1). The following two recommendations were prepared in the mishap investigation report (p. 93 of reference 1):

R.11) Develop a method to measure wing dihedral in real time with a visual display available to the test crew.

R.12) Develop manual or automatic techniques to control wing dihedral in flight.

Geometrically large trim shape sensing for an aircraft during flight is important for a highly flexible aircraft with a high-aspect-ratio wing, such as a high-altitude long endurance aircraft, a transonic truss-braced wing aircraft (The Boeing Company, Chicago, Illinois), and the NASA Ikhana aircraft (General Atomics Aeronautical Systems, Inc., Poway, California). The time history of the terminal event of the NASA Helios aircraft (247-ft wingspan) shows a steady increase in dihedral up to 40 ft (p. 37 of reference 1) (see figure 1) meaning that a large deflection of the wing tip of nearly 32 percent of the wing semi-span occurred before the

mishap. Linear wing shape-sensing techniques can't predict properly such a large structural deformation.

An objective of the jig-shape optimization study for the NASA Low Boom Flight Demonstration mission X-59 Quiet Supersonic Technology (QueSST) aircraft (Lockheed Martin, Bethesda, Maryland) (ref. 2), shown in figure 2, is to minimize the error between the aeroelastic trim shape and the target trim shape at cruise flight speed. The computation of the target trim shape was based on rigid aircraft assumptions. The updated jig-shape is optimum only at the design cruise flight condition, which is the primary limitation of this jig-shape optimization study. When the flight condition and the aircraft weight configuration are changed during flight, the updated jig-shape is "not optimum." The strength of a sonic boom on the ground can be reduced with active trim shape control.

Historically, structural deformation is not easy to measure during flight; however, structural deformation must be measured during flight in order to implement an active shape control technique, such as active dihedral control, active divergence suppression, maneuver load alleviation, gust load alleviation, or active sonic boom control. A linear shape sensing of a flat plate using the measured strain data together with the least-squares surface fitting technique has been introduced by Foss and Haugse (ref. 3). In this approach, the deformation and corresponding strain "mode shapes" were used for the computation of the transformation matrix between the strain input and deformation output. Applications of this approach using strain data measured from fiber-optic strain sensing (FOSS) are observed in (refs. 4 and 5). Deformation computation of aircraft structures using an inverse finite element (FE) method has been introduced by Tessler and Spangler (ref. 6). First, a "simplified" three-dimensional (3D) structural FE model is created in this inverse FE method. Then, errors between measured and computed strain data are minimized using a model tuning technique. Deformations at distributed sensor positions are available from the tuned FE model.

For real-time linear shape sensing, closed-form equations for the computation of structural deformation from the measured strain data have been derived by Ko et al. (ref. 7). Wing deflection along a line is available during flight using systems such as the NASA Armstrong Flight Research Center FOSS. Full-field deformation, however, is not available, and deformation values are only available along the line of the FOSS installation (refs. 8 and 9). The two-step theory for real-time linear shape sensing of a full 3D structure has been introduced by Pak (ref. 10). The first step is the computation of structural deformation along the neutral axis using a numerical integration of curvature based on the linear least-squares method and cubic spline techniques. Curvature along the neutral axis is obtained using strain data and wing thickness information. This curvature is integrated twice to compute deformation along the neutral axis. The second step is to extrapolate deformation along the neutral axis, to the entire aircraft structure to obtain distributed deflection as well as slope information. To date, this linear two-step theory has been demonstrated using simple plate-like structures (refs. 10-12) as well as wings with spars and ribs (ref. 13). Nonlinear shape-sensing techniques have also been introduced (refs. 14-16).

The primary objective of the current study is to introduce a basis function method for predicting linear as well as geometrically nonlinear structural deformation using strain data. Mode shapes, linear static deformation shapes, and geometrically nonlinear static deformation shapes can be used as basis functions in this approach. The proposed method is validated using four example cases.

The Mathematical Background of the Basis Function Method

The approach by Foss and Haugse (ref. 3) requires an analytical model. On the other hand, Ko's closed-form solution (ref. 7) as well as the first step of the two-step theory by Pak (ref. 10) do not need an analytical model. The latter approaches, however, require the deformation and

slope boundary conditions at the starting point of the integration procedure. For most of the cantilevered test articles, it is assumed that the deformation and slope at the wing root section are equal to zero; however, when strain measurement starts in an intermediate position such as the junction between the wing and fuselage, then it is difficult to use zero deformation and slope assumptions. Moreover, errors in boundary conditions will propagate into the rest of the integrations. An analytical model is also needed in the current proposed method; however, it does not require any boundary conditions.

The Basis Function Method

The basis function method in this study is similar to the least-squares surface fitting technique by Foss and Haugse (ref. 3). Assume that the deformation vector, $\{q\}$, in Eq. (1) and strain vector, $\{\epsilon_s\}$, at the strain-gauge positions in equation (2) are defined using the same participation vector, $\{\eta\}$, as follows:

$$\{q\} = [\mathbf{\Phi}]\{\eta\} \tag{1}$$

$$\{\epsilon_s\} = [\mathbf{\Psi_s}]\{\eta\} \tag{2}$$

where columns of the matrix $[\mathbf{\Phi}]$ are the shapes of deformation basis functions. Similarly, the columns of the matrix $[\mathbf{\Psi_s}]$ are the shapes of strain basis functions. Each column of the matrix $[\mathbf{\Phi}]$ corresponds to each column of the matrix $[\mathbf{\Psi_s}]$.

The participation vector $\{\eta\}$ is obtained using the least-squares surface fitting technique. Multiplying the matrix $[\mathbf{\Psi_s}]^{\mathbf{T}}$ to equation (2) gives equation (3) and finally the vector $\{\eta\}$ becomes equation (4).

$$[\mathbf{\Psi_s}]^{\mathbf{T}}\{\epsilon_s\} = [\mathbf{\Psi_s}]^{\mathbf{T}}[\mathbf{\Psi_s}]\{\eta\} \tag{3}$$

$$\{\eta\} = \left([\mathbf{\Psi_s}]^{\mathbf{T}}[\mathbf{\Psi_s}]\right)^{-\mathbf{1}}[\mathbf{\Psi_s}]^{\mathbf{T}}\{\epsilon_s\} \tag{4}$$

Substituting equation (4) into equation (1) gives equation (5).

$$\{q\} = [\mathbf{\Phi}]\left([\mathbf{\Psi_s}]^{\mathbf{T}}[\mathbf{\Psi_s}]\right)^{-\mathbf{1}}[\mathbf{\Psi_s}]^{\mathbf{T}}\{\epsilon_s\} = [\mathbf{T}]\{\epsilon_s\} \tag{5}$$

Therefore, the transformation matrix $[\mathbf{T}]$ from the strain input $\{\epsilon_s\}$ to the deformation output $\{q\}$ becomes as shown in equation (6).

$$[\mathbf{T}] = [\mathbf{\Phi}]\left([\mathbf{\Psi_s}]^{\mathbf{T}}[\mathbf{\Psi_s}]\right)^{-\mathbf{1}}[\mathbf{\Psi_s}]^{\mathbf{T}} \tag{6}$$

The numbers of rows for matrices $[\mathbf{\Phi}]$ and $[\mathbf{\Psi_s}]$ are the total number of deformation degrees of freedom to be measured and the total number of uniaxial strain and shear measurements, respectively. The column number of matrices $[\mathbf{\Phi}]$ and $[\mathbf{\Psi_s}]$ is equal to the number of basis functions used in this transformation.

Candidate basis function shapes in the matrix $[\mathbf{\Phi}]$ can be:

- deformation mode shapes,
- linear static deformation shapes under a variety of load conditions, or
- geometrically nonlinear static deformation shapes under a variety of load conditions.

Therefore, the corresponding strain shapes at the strain-gauge positions in the matrix $[\mathbf{\Psi_s}]$ are obtained. When only the mode shapes are selected as the basis function shapes, then the proposed basis function approach becomes the method developed by Foss and Haugse (ref. 3). In this study, static deformation shapes are also selected as the basis functions.

Computation of Nodal Strain Using the MSC Nastran Code

In the case of the MSC Nastran code (MSC Software, Irvine, California) (ref. 17), the structural deformation and strain values are computed at the nodal and integration points, respectively. However, strain values at nodal points can also be computed using the sample MSC Nastran case control commands shown in table 1. In this table, strain gauges located within the CQUAD4, CTRIA3, CBAR, and CBEAM elements should belong to a surface group. On the other hand, strain gauges on the surface of CHEXA, CPENTA, and CTETRA elements go to a volume group. These case control commands in table 1 can handle one load case at a time.

Computation of Strain at the Strain-Gauge Positions

It is assumed that the deformation sensing and strain-gauge center positions are located inside each FE. Deformation and strain values at any random position inside each FE are computed using the nodal deformation $\{q_i\}$ and nodal strain $\{\epsilon_i\}$ values together with the nodal weighting factors N_i. The deformation and strain vectors $\{q_s\}$ and $\{\epsilon_s\}$ at the deformation sensors and strain gauges are computed using equations (7) and (8):

$$\{q_s\} = \sum_{i=1}^{nn} N_i\{q_i\} \tag{7}$$

$$\{\epsilon_s\} = \sum_{i=1}^{nn} N_i\{\epsilon_i\} \tag{8}$$

where nn is four in the case of CQUAD4, CHEXA, and CPENTA (quadrilateral faces) elements. Similarly, nn is three for CTRIA3, CPENTA (triangular faces), and CTETRA elements and two for CBAR and CBEAM elements.

A coordinate transformation for quadrilateral shapes from the 3D global space to the two-dimensional (2D) local plane is summarized in figure 3. First, as shown in figure 3(b), the four corner nodes in figure 3(a) are transformed into 2D planes. To ensure the uniqueness of the transformation, the first corner node (x_1, y_1, z_1) and second corner node (x_2, y_2, z_2) are located at the origin and on the X axis, respectively, as shown in figure 3(b). The coordinate transformation from the quadrilateral shape in figure 3(b) to the square parent shape in figure 3(c) is performed using the isoparametric shape functions (ref. 18) as shown in equations (9)-(11).

$$X = \sum_{i=1}^{4} N_i(\xi, \eta)\{X_i\} \tag{9}$$

$$Y = \sum_{i=1}^{4} N_i(\xi, \eta)\{Y_i\} \tag{10}$$

$$
\begin{aligned}
N_1(\xi,\eta) &= \frac{(1+\xi)(1+\eta)}{4} \\
N_2(\xi,\eta) &= \frac{(1-\xi)(1+\eta)}{4} \\
N_3(\xi,\eta) &= \frac{(1-\xi)(1-\eta)}{4} \\
N_4(\xi,\eta) &= \frac{(1+\xi)(1-\eta)}{4}
\end{aligned} \tag{11}
$$

Substituting equation (11) into equations (9) and (10) gives equations (12) and (13):

$$4X = a + b\xi + c\eta + d\xi\eta \tag{12}$$

$$4Y = e + f\xi + g\eta + h\xi\eta \tag{13}$$

where, equation (14):

$$
\begin{aligned}
a &= X_1 + X_2 + X_3 + X_4 \\
b &= X_1 - X_2 - X_3 + X_4 \\
c &= X_1 + X_2 - X_3 - X_4 \\
d &= X_1 - X_2 + X_3 - X_4 \\
e &= Y_1 + Y_2 + Y_3 + Y_4 \\
f &= Y_1 - Y_2 - Y_3 + Y_4 \\
g &= Y_1 + Y_2 - Y_3 - Y_4 \\
h &= Y_1 - Y_2 + Y_3 - Y_4
\end{aligned} \tag{14}
$$

The sensor coordinates in the parent element in figure 3(c) are calculated using equations (12)-(14), as well as the coordinates in figure 3(b). Substituting (ξ_s, η_s) values into equation (11) gives the nodal weighting factors for quadrilateral shapes.

The nodal weighting factors for the triangular shapes in figure 4(a) are calculated using an area coordinate in equation (15). Similarly, the nodal weighting factors in equation (16) are used for line shapes in figure 4(b).

$$
\begin{aligned}
N_1 &= \frac{A_1}{A_1 + A_2 + A_3} \\
N_2 &= \frac{A_2}{A_1 + A_2 + A_3} \\
N_3 &= \frac{A_3}{A_1 + A_2 + A_3}
\end{aligned} \tag{15}
$$

$$
\begin{aligned}
N_1 &= \frac{L_1}{L_1 + L_2} \\
N_2 &= \frac{L_2}{L_1 + L_2}
\end{aligned} \tag{16}
$$

Numerical Validation of the Basis Function Method and Discussion

The proposed basis function method is validated in this section using four example cases. These four cases - a high-aspect-ratio wing, a swept test plate, the stabilator of the X-59 QueSST aircraft, and the X-59 QueSST aircraft itself - are discussed below.

The High-aspect-ratio Wing

In this study, the wing shape prediction of a high-aspect-ratio wing with a large dihedral angle is performed. The FE model of this rectangular wing as well as its span and chord lengths are shown in figure 5. The y and z deformations based on the basis function method with mode shapes (ref. 3) and deformation shapes from geometrically nonlinear static analysis as the basis functions are compared with results obtained using the linear (ref. 10) as well as nonlinear two-step theories, as shown in figure 6. The nonlinear two-step theory is explained in the appendix.

First, ten flexible mode shapes are selected for the linear basis function method and the linear two-step theory. On the other hand, 31 nonlinear static deformation shapes under 31 different static load cases are used for the nonlinear basis function method and the nonlinear two-step theory. A total of 810 simulated uniaxial strain data values from the upper and lower skin are used in this sample test.

In general, results from the basis function method have a better correlation with the simulated target values than do the results from the two-step theory. Target deformations are compared with predicted values at the wing-tip location, as shown in table 2. The prediction difference using the nonlinear basis functions is less than 0.3 percent at the wing-tip section. The nonlinear two-step theory (table 2) gives the second-best correlation with the target value, where prediction differences are less than 2.2 percent after the first step and less than 0.5 percent after the second step. The nonlinear two-step theory after the second step gives the same quality of results as the nonlinear basis function method.

In the case of using mode shapes, the basis function method gives better results than does the two-step theory. It should be noted that large prediction differences, 6.13 percent and 14.1 percent, are observed (table 2). These differences are mainly due to the linear assumption of the large deformation.

The Swept Test Plate

The next sample problem is based on the swept test plate shown in figure 7 which was fabricated and tested at the NASA Armstrong Flight Research Center (ref. 8). This test plate has a 45-deg swept angle with a uniform chord and half-span lengths of 12 in and 35.36 in, respectively. Material properties and the FE model of the test plate are given in reference 10. The FOSS layout for the strain data collection is also provided in figure 7.

Sixteen nonlinear static deformations as well as ten mode shapes are selected as basis functions in this example. Static deformations are obtained using 16 different load cases, shown in figure 8. Loading points are shown in figures 7 and 8. Strains and deformations that correspond to load cases 1, 2, and 4 were measured during the test (ref. 8). In this study, load cases 1, 2, and 4 are called the leading-edge load, the uniform load, and the point load, respectively.

The measured plate tip deformations are given in table 3. Three different approaches to shape sensing techniques are compared in this table. These three approaches are the Ko displacement theory (refs. 7 and 8), the two-step theory (ref. 10), and the basis function method. The maximum relative errors from these three approaches are 4.4 percent, 3.8 percent, and 2.3 percent in the case of the leading-edge load case. On the other hand, 3.8 percent, 2.6 percent, and 0.53 percent are observed in the case of the uniform-load case. Finally, the Ko displacement theory is compared with the basis function method in the point-load case. The maximum errors are 5.05 percent and 1.21 percent.

It should be noted that the Ko displacement theory and two-step theory are based on the linear assumption. The basis function method in this example, however, uses nonlinear static deformations as well as mode shapes to capture linear and nonlinear deformations properly.

The fiber lengths along the leading edge, mid chord, and trailing edge are 50 in. Therefore, the maximum deformations divided by fiber length for three load cases are 10.6 percent, 15.9 percent, and 18.1 percent, respectively. Therefore, the first load case is still within the linear range. The second load case is the borderline between the linear and nonlinear range. Finally, the nonlinear deformation is obtained using the third load case.

Relatively large prediction errors at the plate tip in the first linear case might be due to measurement error during the test. In the uniform-load case, the basis function method can handle linear as well as nonlinear cases. In the point-load case, the linear Ko displacement theory creates a larger prediction error than the basis function method. Measured strain and deformation are shown in figures 9. Measured deformations are compared with the computed values in figure 9(b).

The Ko displacement theory (ref. 7) and the first step of the two-step theory (ref. 10) are based on the integration of the curvature along the FOSS line. Therefore, the accuracy of the computed deformation depends on the existence of the stress concentration near the FOSS line (ref. 10). In this swept test plate case, a stress concentration exists near the trailing-edge of the plate root section (ref. 10). High strain values are found from 1 in to 4 in of fiber location, as shown by the green and blue circles in figure 9(a). These high strain values are caused by the stress concentration near the trailing edge of the plate root section.

The basis function method is based on the least-squares surface fitting technique of the measured strain. The quality of the computed deformations under the uniform- and point-load cases is not affected by the local stress concentration as shown in Table 3.

The X-59 Stabilator

The structural shape prediction for the stabilator of the X-59 QueSST aircraft during pre-test analysis is presented in this section. The FE models of the stabilator as well as the positions of the strain-gauge rosettes and the string potentiometers are shown in figure 10. In this example, 30 simulated uniaxial strain data are used, one for each side of the stabilator.

The first 20 flexible mode shapes, 10 for each side of the stabilator, together with seven linear static deformation shapes corresponding to load cases 1 through 7 shown in figure 11, are used as the basis functions in this sample test. These deformation shapes are also used for the simulated target deformation shapes in this section. These seven load cases were used during the proof and calibration tests for the stabilators of the X-59 QueSST aircraft. In this section, three different groups of the basis functions are used for the prediction of the simulated target deformation shapes. Mode shapes and the linear static deformation shapes under different load cases belong to the first and second groups, respectively. The combination of the first and second groups becomes the third group.

Graphical visualizations of the target as well as predicted deformation shapes based on the different basis function groups are shown in figure 12. Comparisons of the target and predicted deformations are also given in table 4. The maximum target deformation for each load case in the second column of table 4 is also provided in figure 12, with black square markers inside black ovals. The maximum prediction differences based on different basis function groups are also provided in table 4. In general, the group 3 basis functions give the smallest percentage difference at the maximum target deformation position, except for load case 1. The maximum differences using the group 3 and 2 basis functions, -0.044 in and -0.047 in, are smaller than the 0.065-in obtained using the group 1 basis functions. The maximum difference position when using group 1 basis functions is at string potentiometer identification number 20, the blue oval in figure 12(a). In this case, the maximum prediction difference is a more meaningful measure of accuracy than comparing the percentage differences.

Participation factors for each load case are summarized in table 5. In this table, basis functions 1 through 7 are obtained from the linear static deformation analysis using the load

cases 1 through 7 in figure 11. On the other hand, basis functions 8 through 27 are the first 20 mode shapes of the stabilator, 10 modes for each side. The mode numbers 1, 2, 4, and 5 on each side of the stabilator are mainly used to fit the target shape when the group 1 basis functions are used. The number of basis functions for group 2, six, is smaller than the group 1 case, 20, even with better prediction performance. It should be noted in this table that the high-frequency mode shapes, modes 18 through 27, do not contribute much to the surface fitting procedures with the group 1 and group 3 cases, mainly due to the surface wiggling of the high-frequency mode shapes. The i-th basis function shouldn't be used for the prediction of the i-th simulated target deformation since these two have the same shape.

The X-59 QueSST Aircraft

The proof test configuration of the X-59 QueSST aircraft is shown in figure 13. The FE model and locations of the strain gauges as well as string potentiometers are shown in figure 14. In this test, string potentiometers are distributed symmetrically, as shown in figure 14 with blue circles. On the other hand, most strain gauges (red circles in figure 14) are located on the left-hand side of the aircraft. The right-hand side strain gauges are mainly located near the main landing gear bay area. There are no strain gauges on the right wing, canards, t-tails, flaps, or ailerons.

The first 30 flexible mode shapes and linear static deformation shapes under 25 different load cases are selected as the basis functions in this example. Three groups of the basis function are also used in this section: (1) group 1 (30 mode shapes); (2) group 2 (25 linear static deformation shapes); and (3) group 3 (group 1 basis functions and group 2 basis functions). The total numbers of uniaxial strain measurements and string potentiometers in figure 14 are 321 and 41, respectively.

When the predicted deformations are compared with the simulated target deformations using load case 2, the basis functions are static deformation shapes under load cases 1 and 3 through 25, as well as 30 mode shapes, as shown in figure 15(a). Table 6 and figure 15(a) show that predicted deformations using group 2 basis functions have an excellent correlation with simulated target deformations. It should be noted that the predicted deformation on the right-hand side of the wing-tip location, at sensor number 26, is still acceptable with the group 2 basis functions, at 8.74 percent, even without any strain gauges on the right-hand side of the wing. The relatively large percentage difference in using the group 3 basis functions, 19.6 percent in Table 6, is mainly caused by the inaccuracy of using the mode shapes for the basis functions, as shown in table 6, 14.2 percent. The prediction difference at the left-hand side of the wing tip, 4.25 percent, is much smaller than the prediction difference at the right-hand side of the wing tip.

Structural deformations of the X-59 QueSST aircraft are computed using measured strain data from the proof test. It should be noted that the strain-gauge locations in this study are selected to verify the load equation for the future flight test, not for structural shape sensing. Figure 15(b) compares predicted and measured structural deformations. In general, the group 2 basis functions give the best correlation with the target values. Large shape-sensing differences are mainly observed on structural components without strain gauges, such as the right wing, canards, and T-tails. It should be noted that the group 2 basis functions produce reasonable results at sensor numbers 25 and 26 on the right-hand side of the wing tip, as shown in figure 15(b). Basis functions based on mode shapes give an unusable deformation prediction with 83.7-percent and 149-percent errors. The maximum prediction difference with the group 2 basis functions is at the right canard position, -0.828 in at sensor number 11. Strain gauges are not installed on the canard surfaces as shown in Fig. 14.

Conclusions

A basis function method for linear and geometrically nonlinear structural shape sensing is proposed in this study. Basis functions can be mode shapes, linear static deformation shapes, or geometrically nonlinear static deformation shapes. The proposed basis function method is validated using a high-aspect-ratio wing. The prediction difference using the nonlinear basis functions is less than 0.3 percent at the wing-tip section.

The swept test plate with a stress concentration is also selected as a sample case. Integration-based shape sensing techniques are affected by the presence of a stress concentration. The basis function method gives excellent deformation prediction, even with stress concentration.

Performance of the basis functions using mode shapes and static deformation is compared using the sample case from the stabilator of the National Aeronautics and Space Administration Low-Boom Demonstration mission X-59 Quiet Supersonic Technology (QueSST) aircraft (Lockheed Martin, Bethesda, Maryland). In most of the sample load cases, excepting load case 1, the static deformations give better prediction performance than do the mode shapes. In load case 1, the prediction error using the group 1 basis functions is smaller than the results obtained using the group 2 and group 3 basis functions at the same sensor location. When the prediction errors at all the string potentiometer locations are compared, however, the group 1 basis functions give the worst performance. Mainly, the mode shapes of the low-frequency modes participate in structural shape sensing.

Wing shape sensing with sparse strain data is also demonstrated in this study using the X-59 QueSST aircraft. Strain gauges are not installed on the right wing, canards, t-tails, flaps, or ailerons. The maximum prediction errors using the group 1 and group 3 basis functions at the sensor identification number 26 location (the right wing-tip section) are 3.769 in (83.7-percent error) and 6.731 in (149-percent error), respectively. On the other hand, the maximum prediction error using the group 2 basis function is 0.557 in (12.4-percent error) at the same string potentiometer location. The predicted deformations have a good match with the target deformations.

Appendix: Geometrically Nonlinear Two-Step Theory

A block diagram of the mathematical background of the two-step theory[1] is shown in figure A-1. All three blocks are about the first step, except the upper right block, which is the second step. The first step of the nonlinear two-step theory can be summarized as follows:

Step 1: Take axial strain measurements along each fiber-optic strain sensing (FOSS) line. A strain on one side and corresponding strain on the other side of the structure are needed to compute the curvature.

Step 2: Compute the curvature along the neutral axis. Multiple straight bar elements should be defined along the FOSS line. The centroids of elements should match the strain measuring points. Assume that each element is under constant strain. In each bar element, compute the curvature defined in equation (A-1). The curvature along the neutral axis is defined in figure A-2.

$$\kappa = -\frac{\epsilon_u - \epsilon_l}{h} = \frac{d^2 w(\tilde{s})}{d\tilde{s}^2} \tag{A-1}$$

Step 3: Compute the slope and deformation along the neutral axis. Integrate equation (A-1), then the slope is available, equation (A-2).

$$\frac{dw(\tilde{s})}{d\tilde{s}} \tag{A-2}$$

When equation (A-2) is integrated, the linear deformation in the fiber direction, $w(\tilde{s})$ shown in figure A-3(a), is obtained. Therefore, geometrically nonlinear deformation, $\Delta\tilde{s}$ and $\Delta\tilde{z}$ in "fiber coordinates," can be computed.

Step 4: A local dihedral, anhedral, or taper effect, angle α in figure A-3(b), should be included in the deformation computation. Rotate the deformation $\Delta\tilde{s}$ and $\Delta\tilde{z}$ to have Δs and Δz in figure A-3(b).

Step 5: Finally, in figure A-3(c), include the curved fiber effect, angle β. Calculate the deformation Δx and Δy from Δs.

In the second step, computed deformations from the first step are expanded to the entire structure using the System Equivalent Reduction and Expansion Process (SEREP).[2] Rearrange all the degrees of freedom (DOF) in the finite element model, as equation (A-3):

$$\{q\} = \begin{Bmatrix} q_M \\ q_S \end{Bmatrix} \tag{A-3}$$

where $\{q_M\}$ is the master DOF. In this approach, deformations from the first step are defined as the master DOF. The rest of the deformations all over the structure are defined as slave DOF, $\{q_S\}$. Consider the following coordinate transformation for the model reduction and expansion techniques as equation (A-4):

---

[1] Pak, Chan-gi, "Wing Shape Sensing from Measured Strain," *AIAA Journal*, vol. 54, no. 3, March 2016, pp. 1064-1073.

[2] O'Callahan, J., Avitabile, P., and Riemer, R., "System Equivalent Reduction Expansion Process," *Proceedings of the 7th International Modal Analysis Conference*, Las Vegas, Nevada, 1989, pp. 29-37.

$$\begin{Bmatrix} q_M \\ q_S \end{Bmatrix} = [\mathbf{T}]\{\tilde{q}_M\} \tag{A-4}$$

where $\{\tilde{q}_M\}$ is the measured master DOF which was computed from the first step. From SEREP, the transformation matrix $[\mathbf{T}]$ can be expressed as equation (A-5):

$$[\mathbf{T}] = \begin{bmatrix} \Phi_{\mathbf{M}}\left(\Phi_{\mathbf{M}}^{\mathbf{T}}\Phi_{\mathbf{M}}\right)^{-\mathbf{1}}\Phi_{\mathbf{M}}^{\mathbf{T}} \\ \Phi_{\mathbf{S}}\left(\Phi_{\mathbf{M}}^{\mathbf{T}}\Phi_{\mathbf{M}}\right)^{-\mathbf{1}}\Phi_{\mathbf{M}}^{\mathbf{T}} \end{bmatrix} \tag{A-5}$$

where $\Phi_{\boldsymbol{M}}$ and $\Phi_{\boldsymbol{S}}$ are basis functions corresponding to master and slave DOFs, respectively. These basis functions are mode shapes and/or static deformation shapes. From equations (A-3) through (A-5), all the DOF in the structure can be computed using equation (A-6):

$$\{q\} = \begin{Bmatrix} q_M \\ q_S \end{Bmatrix} = \begin{bmatrix} \Phi_{\boldsymbol{M}}\left(\Phi_{\boldsymbol{M}}^{\mathbf{T}}\Phi_{\boldsymbol{M}}\right)^{-\mathbf{1}}\Phi_{\boldsymbol{M}}^{\mathbf{T}} \\ \Phi_{\boldsymbol{S}}\left(\Phi_{\boldsymbol{M}}^{\mathbf{T}}\Phi_{\boldsymbol{M}}\right)^{-\mathbf{1}}\Phi_{\boldsymbol{M}}^{\mathbf{T}} \end{bmatrix}\{\tilde{q}_M\} \tag{A-6}$$

References

1. Noll, Thomas E., John M. Brown, Marla E. Perez-Davis, Stephen D. Ishamael, Geary C. Tiffany, and Matthew Gaier, *Investigation of the Helios Prototype Aircraft Mishap, Volume I Mishap Report,* NASA, 2004.

2. Pak, Chan-gi, “Jig-Shape Optimization of Low-Boom Supersonic Aircraft,” *Journal of Aircraft,* vol. 55, no. 5, 2018, pp. 2154-2161.

3. Foss, G. C. and E. D. Haugse, “Using Modal Test Results to Develop Strain to Displacement Transformations,” *Proceedings of the 13th International Modal Analysis Conference,* 1995, pp. 112-118.

4. Kang, Lae-Hyong, Dae-Kwan Kim, and Jae-Hung Han, “Estimation of dynamic structural displacements using fiber Bragg grating strain sensors,” *Journal of Sound and Vibration,* vol. 305, no. 3, 2007, pp. 534-542.

5. Freydin Maxim, Miko Keren Rattner, Daniella Raveh, Iddo Kressel, Roy Davidi, and Moshe Tur, “Fiber-Optics-Based Aeroelastic Shape Sensing,” *AIAA Journal,* vol. 57, no. 12, December 2019, pp. 5094-5103.

6. Tessler, Alexander, and Jan L. Spangler, *A Variational Principle for Reconstruction of Elastic Deformations in Shear Deformable Plates and Shells,* NASA/TM-212445, 2003.

7. Ko, William L., W. L. Richards, and Van T. Tran, *Displacement Theories for In-Flight Deformed Shape Predictions of Aerospace Structures,* NASA/TP-2007-214612, 2007.

8. Bakalyar, John, and Christine Jutte, “Validation Tests of Fiber Optic Strain-Based Operational Shape and Load Measurements,” AIAA Paper 2012-2904, 2012.

9. Armen Derkevorkian, Sami F. Masri, Jessica Alvarenga, Helen Boussalis, John Bakalyar, and W. Lance Richards, “Strain-Based Deformation Shape-Estimation Algorithm for Control and Monitoring Applications,” *AIAA Journal,* vol. 51, no. 9, September 2013, pp. 2231-2240.

10. Pak, Chan-gi, “Wing Shape Sensing from Measured Strain,” *AIAA Journal,* vol. 54, no. 3, March 2016, pp. 1064-1073.

11. Pak, Chan-gi, and Roger Truax, “Acceleration and Velocity Sensing from Measured Strain,” AIAA Paper 2016-1229, 2016.

12. Pak, Chan-gi, “Unsteady Aerodynamic Force Sensing from Strain Data,” *Journal of Aircraft,* vol. 54, no. 4,July-August 2017, pp. 1476-1485.

13. Pak, Chan-gi, “Shape Sensing for Wings with Spars and Ribs using Simulated Strain,” AIAA Paper 2019-1756, 2019.

14. Su, Weihua, and Carlos E. S. Cesnik, “Nonlinear Aeroelasticity of a Very Flexible Blended-Wing-Body Aircraft," *AIAA Journal,* vol. 47, no. 5, September-October 2010, pp. 1539-1553.

15. Ko, William L., Van Tran Fleischer, and Shun-fat Lung, *Curved Displacement Transfer Functions for Geometric Nonlinear Large Deformation Structure Shape Predictions,* NASA/TP-2017-219406, 2017.

16. Drachinsky, Ariel, and Daniella E. Raveh, “Modal Rotations: A Modal-Based Method for Large Structural Deformations of Slender Bodies," *AIAA Journal,* vol. 58, no. 7, July 2020, pp. 3159-3173.

17. *MSC Nastran 2018 Quick Reference Guide,* MacNeal-Schwendler Corp., Newport Beach, California, 2017.

18. Zienkiewicz, O. C., *The Finite Element Method, Third Edition,* McGraw-Hill, 1977.

Tables

Table 1. Case control commands for printing strain results at the nodal points (ref. 17).

Case control commands	**Comments**
SET n=#1, #2, … #k, … etc.	n: Set identification number for printing results #k: Set identification number of surfaces and volumes
Strain(corner,fiber)=all	Results under this command will be based on **element coordinate system** Corner: Output element strains at the center and grid points. Fiber: Strain at locations Z1, Z2, and MID are computed for plate elements. • Z1: lower surface of a plate element (based on the surface normal direction) • Z2: upper surface of a plate element (based on the surface normal direction) • MID: middle plane of a plate element
GPSTRAIN=n	Results under this command will be based on each SURFACE and VOLUME (**local coordinate system CORD #m**) n: Set identification number of a **previously appearing SET command**. Only surfaces and volumes with identification numbers that appear on this SET command will be included in the grid point strain output request
OUTPUT(post)	This command must precede all SURFACE and VOLUME commands.
SET #k=#1, #2, … #j, … etc.	#k: Set identification number of surfaces and volumes #j: Element identification numbers belong to SET #k group
SURFACE #i, SET #k, SYSTEM CORD #m, AXIS X	Defines a surface for the calculation of grid point strains #i: Surface identification number #k: Set identification number of surfaces #m: Local coordinate system identification number Axis: Specifies the axis of the coordinate system to be used as the **x output axis** and the **local x-axis** when geometric interpolation is used.
VOLUME #i, SET #k, SYSTEM CORD #m	Defines a volume for the calculation of grid point strains. #i: Volume identification number #k: Set identification number of volumes #m: Local coordinate system identification number

Table 2. Wing-tip deformation of high-aspect-ratio rectangular wing box.

Deformation	**Target**	**Basis function method**				**Two-step theory**					
		Nonlinear		Linear		Nonlinear (after step 1)		Nonlinear (after step2)		Linear	
		Value	diff., %	Value	diff., %	Value	diff., %	Value	diff., %	Value	diff., %
Y, in	-36.35	-36.25	**-0.29**	-34.12	-6.13	-35.71	**-1.77**	-36.30	**-0.15**	-31.21	-14.1
Z, in	51.19	51.12	**-0.14**	52.45	2.46	50.12	**-2.11**	50.97	**-0.43**	54.06	5.60

Table 3. Test plate deformation at plate tip.

Fiber location	Measured, in	Computed, in			Relative error, %		
		Bakalyar & Jutte*	Two-step method**	Basis function	Bakalyar & Jutte*	Two-step method**	Basis function
Leading-edge load (load case 1)							
Leading-edge fiber	-4.525	-4.500	-4.569	-4.493	-0.55	0.97	-0.72
Middle fiber	-4.912	-4.952	-4.843	-4.835	0.81	-1.40	-1.57
Trailing-edge fiber	-5.300	-5.067	-5.097	-5.180	**-4.40**	**-3.80**	**-2.25**
Uniform-load (load case 2)							
Leading-edge fiber	-6.541	-6.546	-6.684	-6.549	0.08	2.20	0.12
Middle fiber	-7.256	-7.408	-7.238	-7.234	2.10	-0.25	-0.30
Trailing-edge fiber	-7.971	-7.667	-7.763	-7.929	**-3.80**	**-2.60**	**-0.53**
Point load at trailing edge of plate tip (load case 4)							
Leading-edge fiber	-7.087	-7.007	N/A	-7.172	-1.13	N/A	**1.21**
Middle fiber	-8.073	-8.145	N/A	-8.140	0.89	N/A	0.83
Trailing-edge fiber	-9.058	-8.601	N/A	-9.137	**-5.05**	N/A	0.87

*: Reference (8)
**: Reference (10)

Table 4. Comparisons of Z deformation using different basis functions.

Load Case	Max. target deform.* (Pot. ID #)	Group 1 (mode shapes: 20)		Group 2 (static shapes: 6)		Group 3 (static + mode shapes: 26)	
		Difference** (% diff.)	Max. Diff.† (Pot. ID #)	Difference (% diff.)	Max. Diff. (Pot. ID #)	Difference (% diff.)	Max. Diff. (Pot. ID #)
1	-0.643 (3)	0.004 (**-0.6**)	**0.065** (20)	-0.047 (**7.3**)	**-0.047** (**3**)	-0.044 (**6.8**)	**-0.044** (**3**)
2	1.213 (20)	-0.078 (**-6.5**)	-0.078 (**20**)	0.022 (**1.8**)	0.022 (**20**)	0.001 (**0.1**)	-0.008 (3)
3	3.647 (10)	-0.172 (**-4.7**)	-0.174 (20)	0.020 (**0.5**)	-0.021 (13)	0.010 (**0.3**)	0.046 (3)
4	-1.372 (20)	0.070 (**-5.1**)	0.070 (**20**)	0.031 (**-2.3**)	0.035 (10)	0.006 (**-0.4**)	-0.010 (9)
5	0.713 (20)	0.024 (**3.4**)	0.026 (10)	0.018 (**2.5**)	0.021 (10)	0.006 (**0.8**)	0.006 (**20**)
6	2.712 (10)	-0.060 (**-2.2**)	-0.060 (**10**)	-0.020 (**-0.7**)	-0.020 (**10**)	-0.007 (**-0.3**)	-0.017 (3)
7	2.712 (20)	-0.060 (**-2.2**)	-0.060 (**20**)	-0.016 (**-0.6**)	-0.016 (**20**)	-0.007 (**-0.3**)	-0.017 (13)

*: inch
**: Difference (inch) at the maximum target deformation
†: Maximum difference of the measured deformation

Table 5. Participation factors of each basis function.

Basis func. #	Load case 1			Load case 2			Load case 3			Load case 4			Load case 5			Load case 6			Load case 7		
	Group 1	Group 2	Group 3	Group 1	Group 2	Group 3	Group 1	Group 2	Group 3	Group 1	Group 2	Group 3	Group 1	Group 2	Group 3	Group 1	Group 2	Group 3	Group 1	Group 2	Group 3
1	0.0	0.0	0.0	0.0	0.0	0.0	0.0	-0.3	0.7	0.0	-0.2	0.3	0.0	-0.1	0.1	0.0	0.2	-0.3	0.0	0.2	-0.3
2	0.0	-0.3	-0.2	0.0	0.0	0.0	0.0	-0.2	0.3	0.0	-1.2	-0.6	0.0	-0.5	-0.8	0.0	0.4	0.7	0.0	0.4	0.7
3	0.0	-2.4	1.0	0.0	-0.1	0.0	0.0	0.0	0.0	0.0	-0.7	-0.3	0.0	-0.4	-0.2	0.0	0.6	0.5	0.0	0.6	0.5
4	0.0	-1.5	2.0	0.0	-0.6	-0.5	0.0	-0.6	-1.5	0.0	0.0	0.0	0.0	-0.4	-0.7	0.0	0.5	1.1	0.0	0.5	1.1
5	0.0	-1.6	1.0	0.0	-0.8	-0.7	0.0	-1.2	-1.0	0.0	-1.5	-0.8	0.0	0.0	0.0	0.0	1.1	1.1	0.0	1.1	1.2
6	0.0	3.0	-1.4	0.0	0.5	0.3	0.0	1.4	1.4	0.0	1.3	0.7	0.0	0.8	0.6	0.0	0.0	0.0	0.0	-1.0	-1.0
7	0.0	3.0	-1.4	0.0	0.5	0.3	0.0	1.4	1.4	0.0	1.3	0.7	0.0	0.8	0.6	0.0	-1.0	-1.0	0.0	0.0	0.0
8	0.2	0.0	1.6	0.8	0.0	0.1	2.8	0.0	-1.3	-0.7	0.0	-0.5	0.8	0.0	-0.2	0.0	0.0	0.6	2.5	0.0	0.6
9	0.2	0.0	1.6	0.8	0.0	0.1	2.8	0.0	-1.3	-0.7	0.0	-0.5	0.8	0.0	-0.2	2.5	0.0	0.6	0.0	0.0	0.5
10	-0.7	0.0	0.2	0.5	0.0	0.0	1.1	0.0	-0.1	-0.7	0.0	-0.1	-0.1	0.0	-0.1	0.0	0.0	0.1	0.3	0.0	0.1
11	-0.7	0.0	0.3	0.6	0.0	0.0	1.1	0.0	-0.1	-0.7	0.0	-0.1	-0.1	0.0	-0.1	0.3	0.0	0.1	0.0	0.0	0.1
12	0.0	0.0	0.0	0.0	0.0	0.0	0.0	0.0	0.0	0.0	0.0	0.0	0.0	0.0	0.0	0.0	0.0	0.0	0.0	0.0	0.0
13	0.0	0.0	0.0	0.0	0.0	0.0	0.0	0.0	0.0	0.0	0.0	0.0	0.0	0.0	0.0	0.0	0.0	0.0	0.0	0.0	0.0
14	0.1	0.0	-0.1	-0.1	0.0	0.0	0.0	0.0	0.1	0.1	0.0	0.0	0.1	0.0	0.0	0.0	0.0	0.0	0.1	0.0	0.0
15	0.1	0.0	-0.1	-0.1	0.0	0.0	0.0	0.0	0.1	0.1	0.0	0.0	0.1	0.0	0.0	0.1	0.0	0.0	0.0	0.0	0.0
16	0.3	0.0	0.2	-0.1	0.0	0.0	-0.1	0.0	-0.2	0.1	0.0	-0.1	0.1	0.0	0.0	0.1	0.0	0.1	0.0	0.0	0.1
17	0.3	0.0	0.2	-0.1	0.0	0.0	-0.1	0.0	-0.2	0.1	0.0	-0.1	0.1	0.0	0.0	0.0	0.0	0.1	0.1	0.0	0.1
18	-0.1	0.0	0.0	0.0	0.0	0.0	0.1	0.0	0.0	0.0	0.0	0.0	0.0	0.0	0.0	0.0	0.0	0.0	0.0	0.0	0.0
19	-0.1	0.0	0.0	0.0	0.0	0.0	0.1	0.0	0.0	0.0	0.0	0.0	0.0	0.0	0.0	0.0	0.0	0.0	0.0	0.0	0.0
20	0.0	0.0	0.0	0.0	0.0	0.0	0.0	0.0	0.0	0.0	0.0	0.0	0.0	0.0	0.0	0.0	0.0	0.0	0.0	0.0	0.0
21	0.0	0.0	0.0	0.0	0.0	0.0	0.0	0.0	0.0	0.0	0.0	0.0	0.0	0.0	0.0	0.0	0.0	0.0	0.0	0.0	0.0
22	0.0	0.0	0.0	0.0	0.0	0.0	0.0	0.0	0.0	0.0	0.0	0.0	0.0	0.0	0.0	0.0	0.0	0.0	0.0	0.0	0.0
23	0.0	0.0	0.0	0.0	0.0	0.0	0.0	0.0	0.0	0.0	0.0	0.0	0.0	0.0	0.0	0.0	0.0	0.0	0.0	0.0	0.0
24	0.1	0.0	0.0	0.0	0.0	0.0	-0.1	0.0	0.0	0.0	0.0	0.0	0.0	0.0	0.0	0.0	0.0	0.0	0.0	0.0	0.0
25	0.0	0.0	0.0	0.0	0.0	0.0	-0.1	0.0	0.0	0.0	0.0	0.0	0.0	0.0	0.0	0.0	0.0	0.0	0.0	0.0	0.0
26	0.0	0.0	0.0	0.0	0.0	0.0	0.0	0.0	0.0	0.0	0.0	0.0	0.0	0.0	0.0	0.0	0.0	0.0	0.0	0.0	0.0
27	0.0	0.0	0.0	0.0	0.0	0.0	0.0	0.0	0.0	0.0	0.0	0.0	0.0	0.0	0.0	0.0	0.0	0.0	0.0	0.0	0.0

Table 6. Comparisons of Z deformation using different basis functions for load case 2.

Target Deform.	**Max. target deform. (PID #)**	**Deform. at mirror image location of max. target deform. (PID #)**	**Group 1 (mode shapes: 30)**		**Group 2 (static shapes: 24)**		**Group 3 (group 1+ group 2)**	
			Diff. (% diff.)	**Max. Diff. (PID #)**	**Diff. (% diff.)**	**Max. Diff. (PID #)**	**Diff. (% diff.)**	**Max. Diff. (PID #)**
Simulated	4.104 (26)		0.581 (**14.2**)	**0.581** (26)	0.359 (**8.74**)	**0.359** (26)	0.804 (**19.6**)	**0.804** (26)
		4.099 (19)	0.578 (14.1)		0.174 (**4.25**)		0.004 (0.10)	
Measured		4.501 (26)	3.769 (83.7)	**3.769** (26)	**-0.557** (-12.37)	**-0.828** (11)	6.731 (149.)	**6.731** (26)
	4.554 (19)		-0.050 (-1.09)		-0.411 (-9.02)		-0.278 (-6.11)	

Deform. = Deformation
Diff. (inch) = Difference between target deformation and predicted deformation
Max. = Maximum
PID #: String potentiometer identification number
PID 19: left wing tip, strain gauges are located
PID 26: right wing tip, **strain gauges are not located**
PID 11: right forward outboard canard**, strain gauges are not located**

Figures

(a) During takeoff

(b) Before the mishap

220036

Figure 1. The Helios aircraft (AeroVironment, Arlington, Virginia): (a) during takeoff; and (b) before the mishap.

Figure 2. The X-59 Quiet Supersonic Technology (QueSST) aircraft (Lockheed Martin, Bethesda, Maryland).

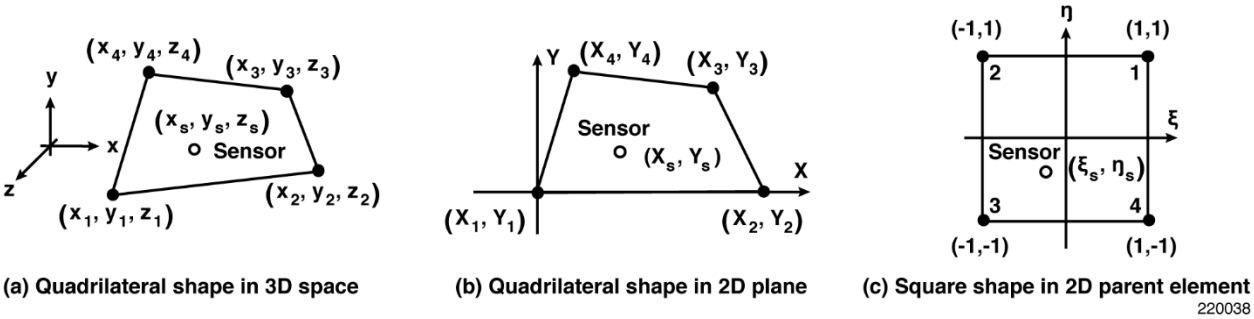

Figure 3. Coordinate transformation for quadrilateral shapes.

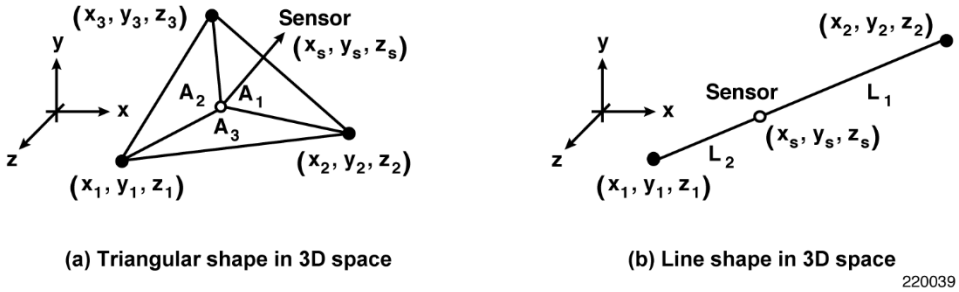

Figure 4. Area and length coordinates for triangular and line shapes.

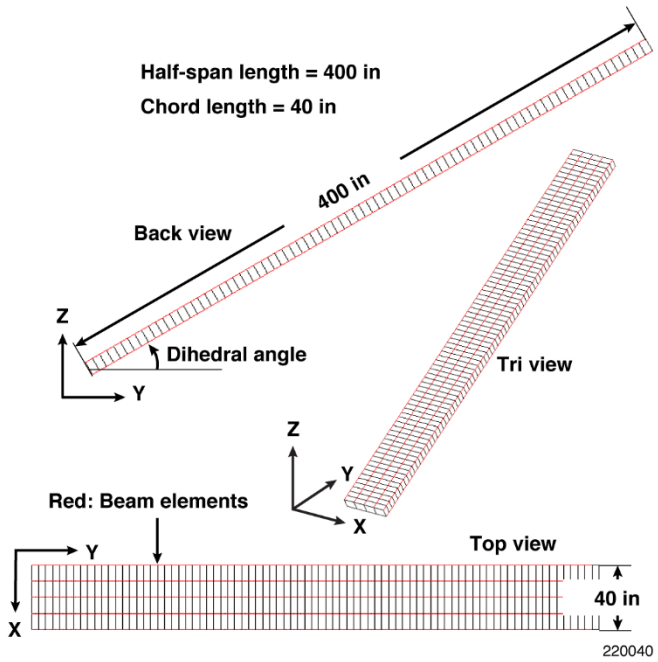

Figure 5. The finite-element model of the high-aspect-ratio rectangular wing.

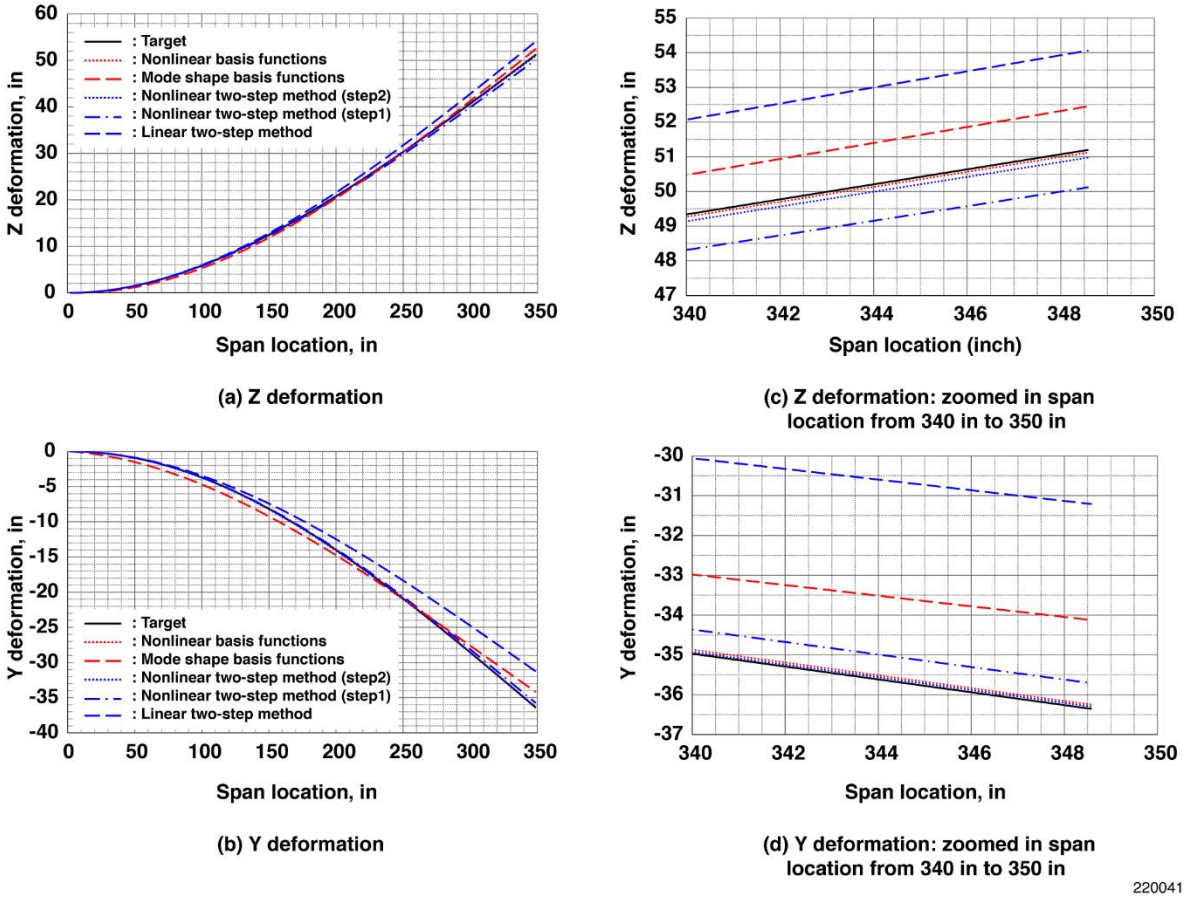

Figure 6. Comparisons of structural shape-sensing techniques using a rectangular wing model.

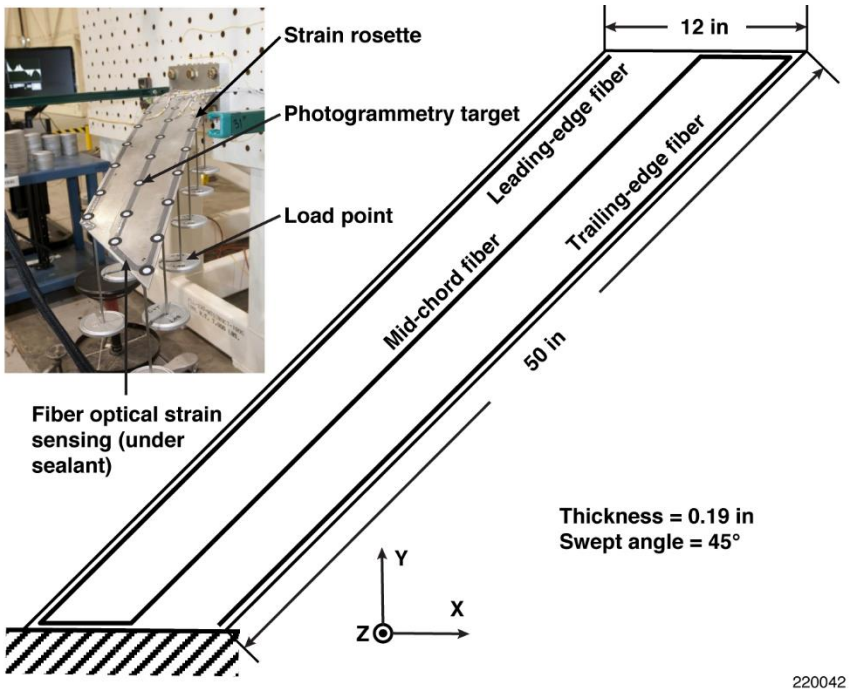

Figure 7. Swept test plate.

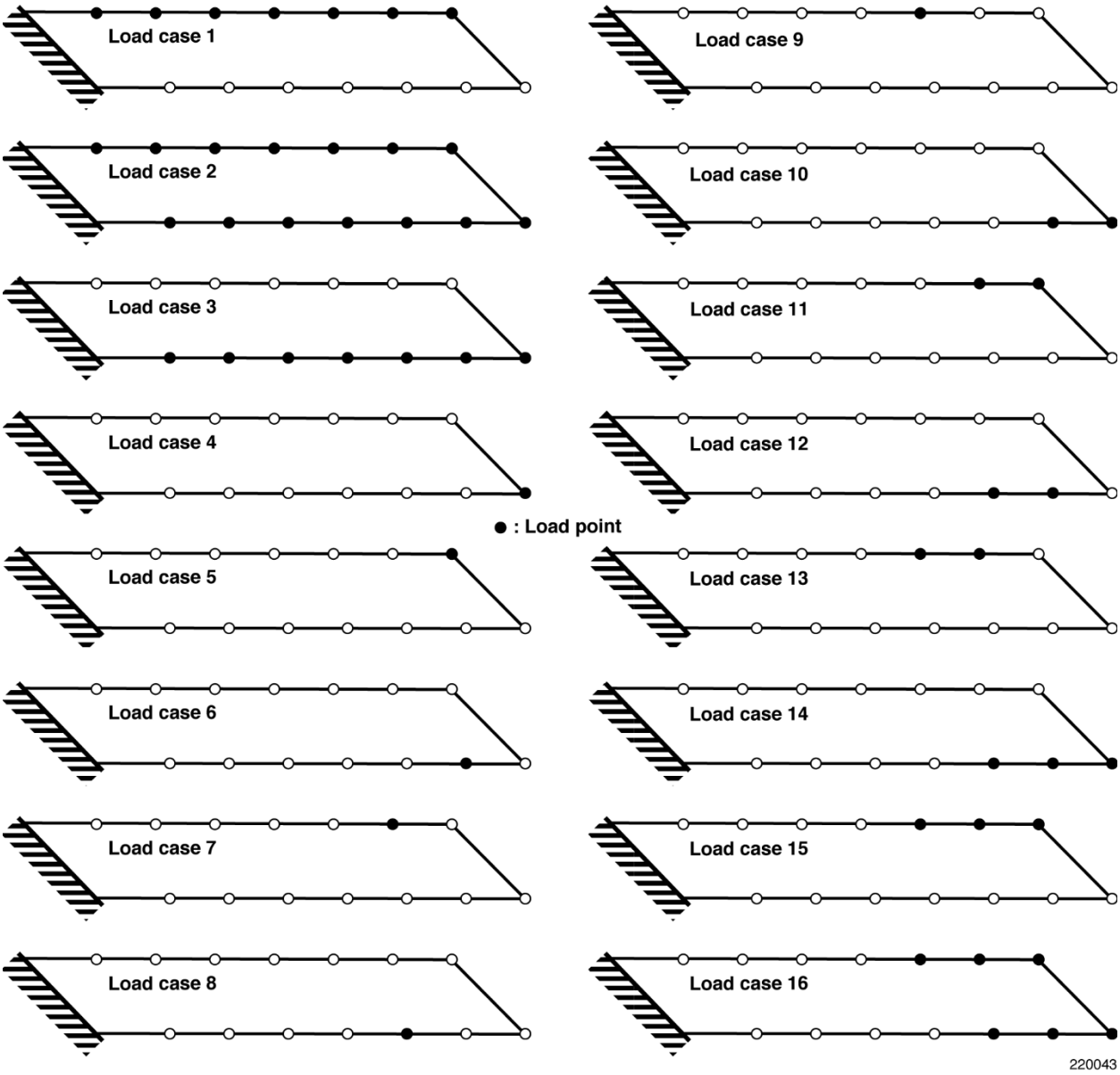

Figure 8. Load cases for generating basis functions.

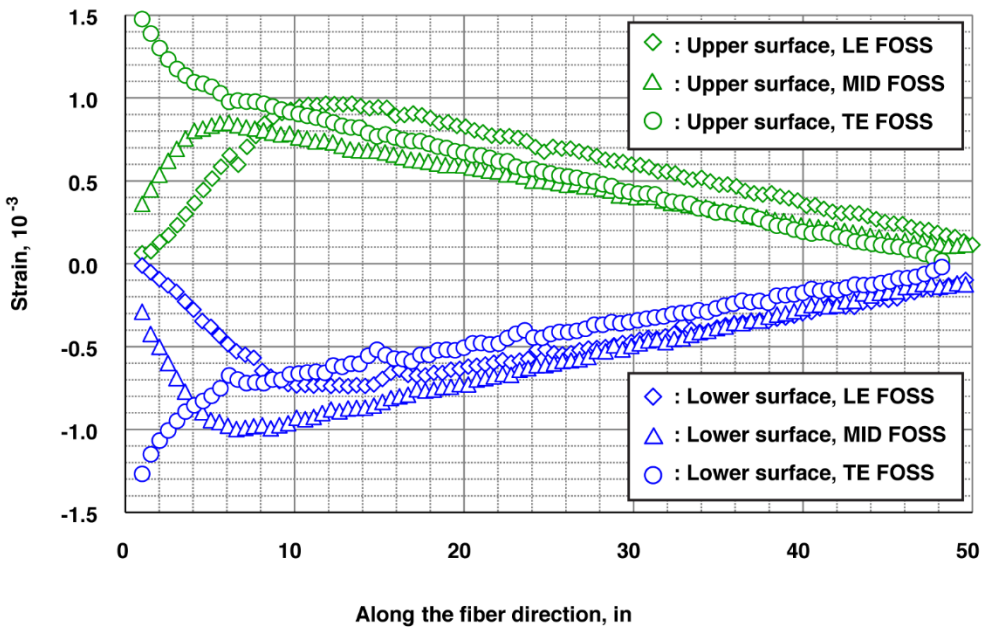

(a) Measured strain

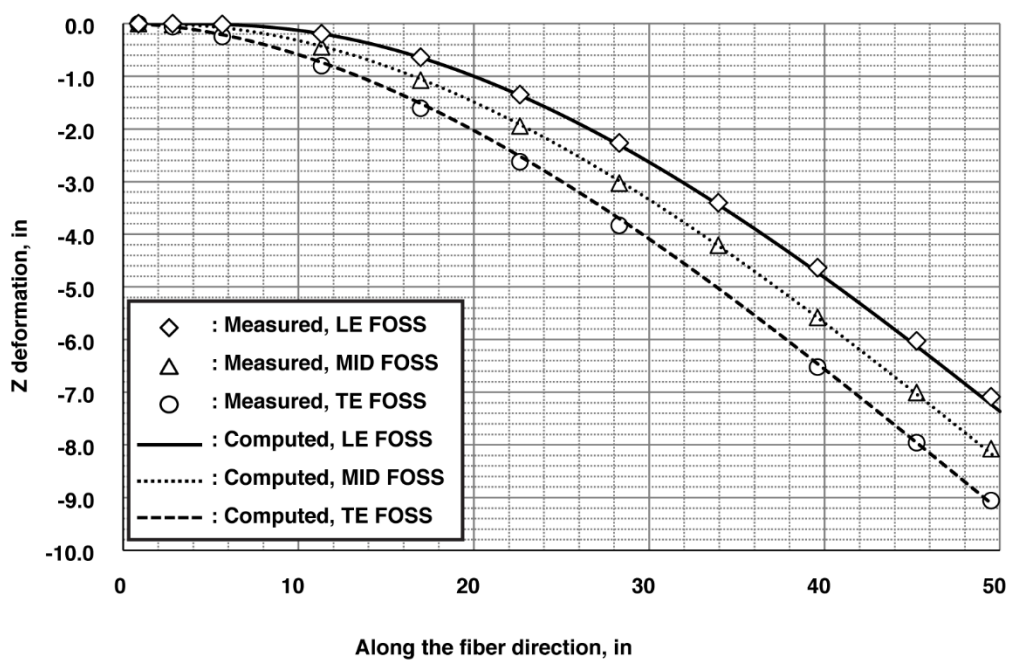

(b) Deformation

220044

Figure 9. Measured strain and deformation of the test plate under a point-load case.

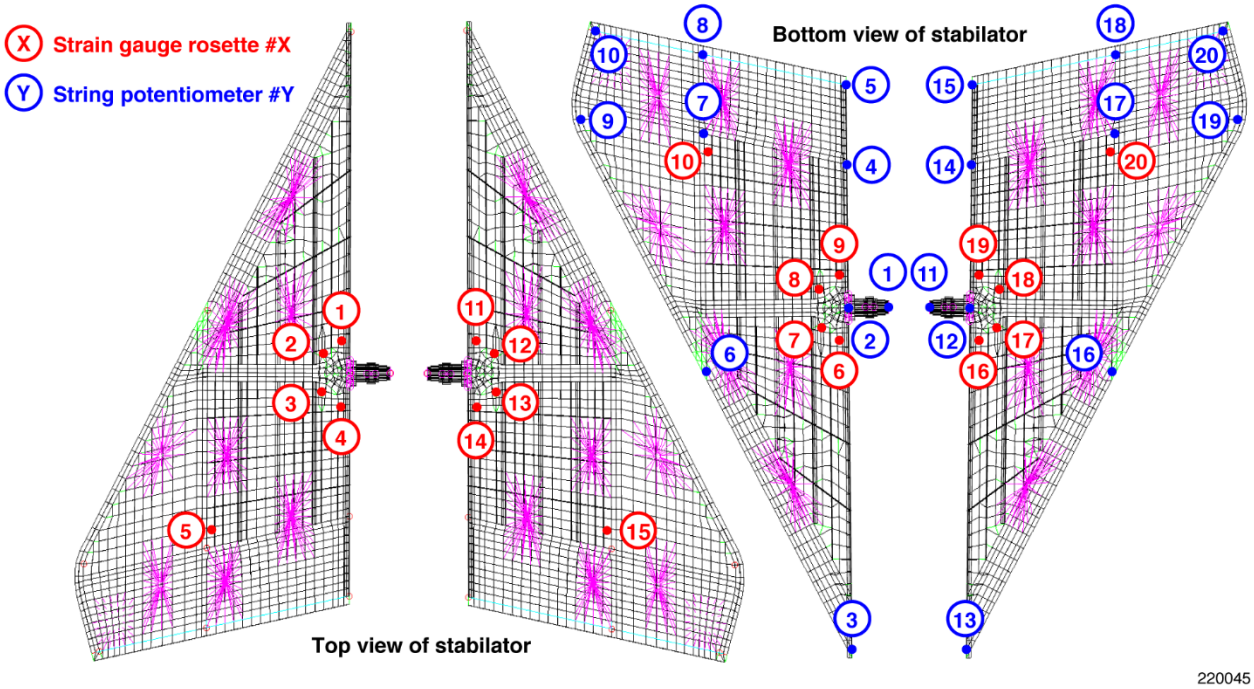

Figure 10. Positions of strain-gauge rosettes and string potentiometers for the X-59 stabilator.

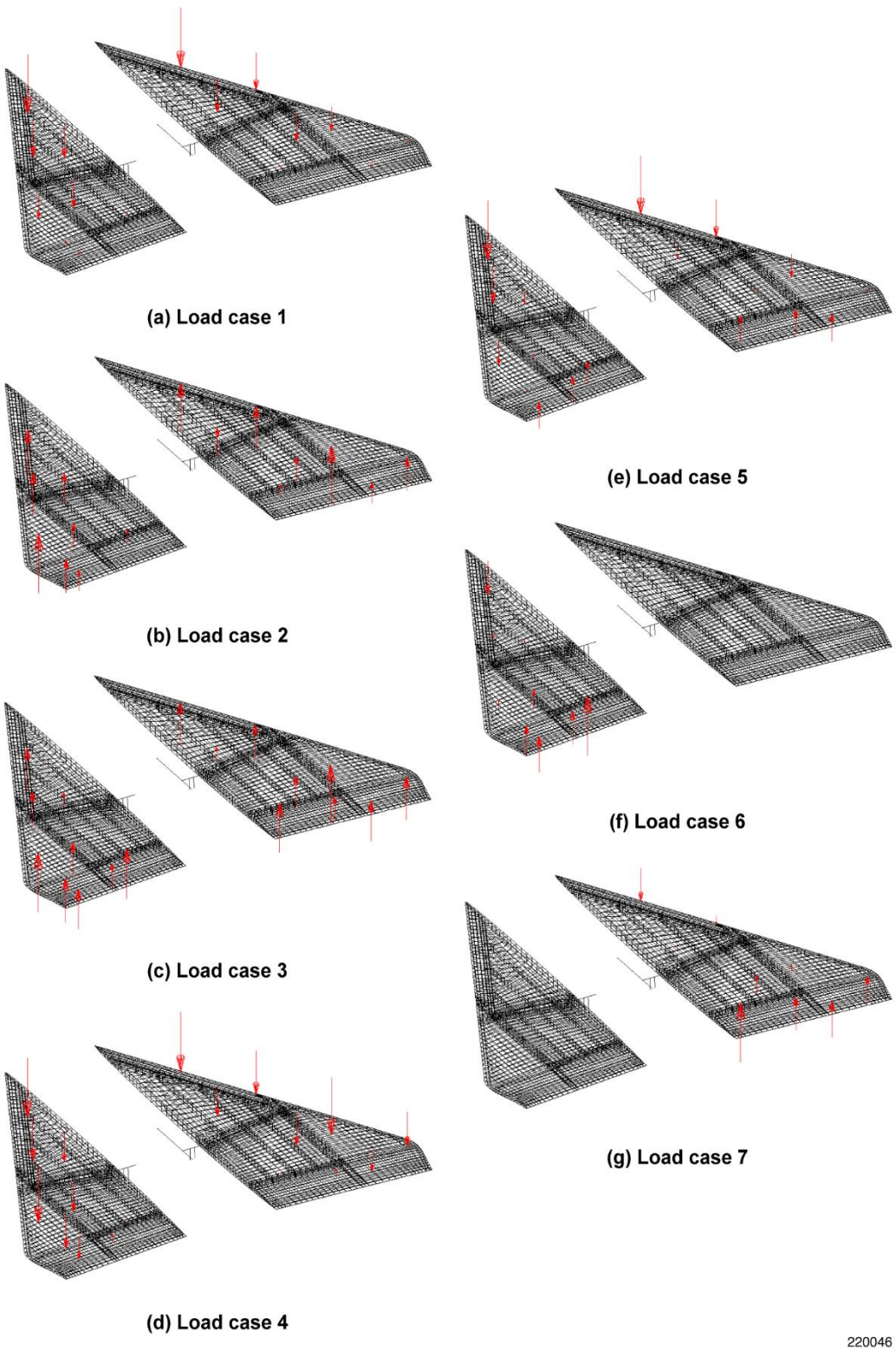

Figure 11. Seven load cases for the generation of the target and basis function shapes.

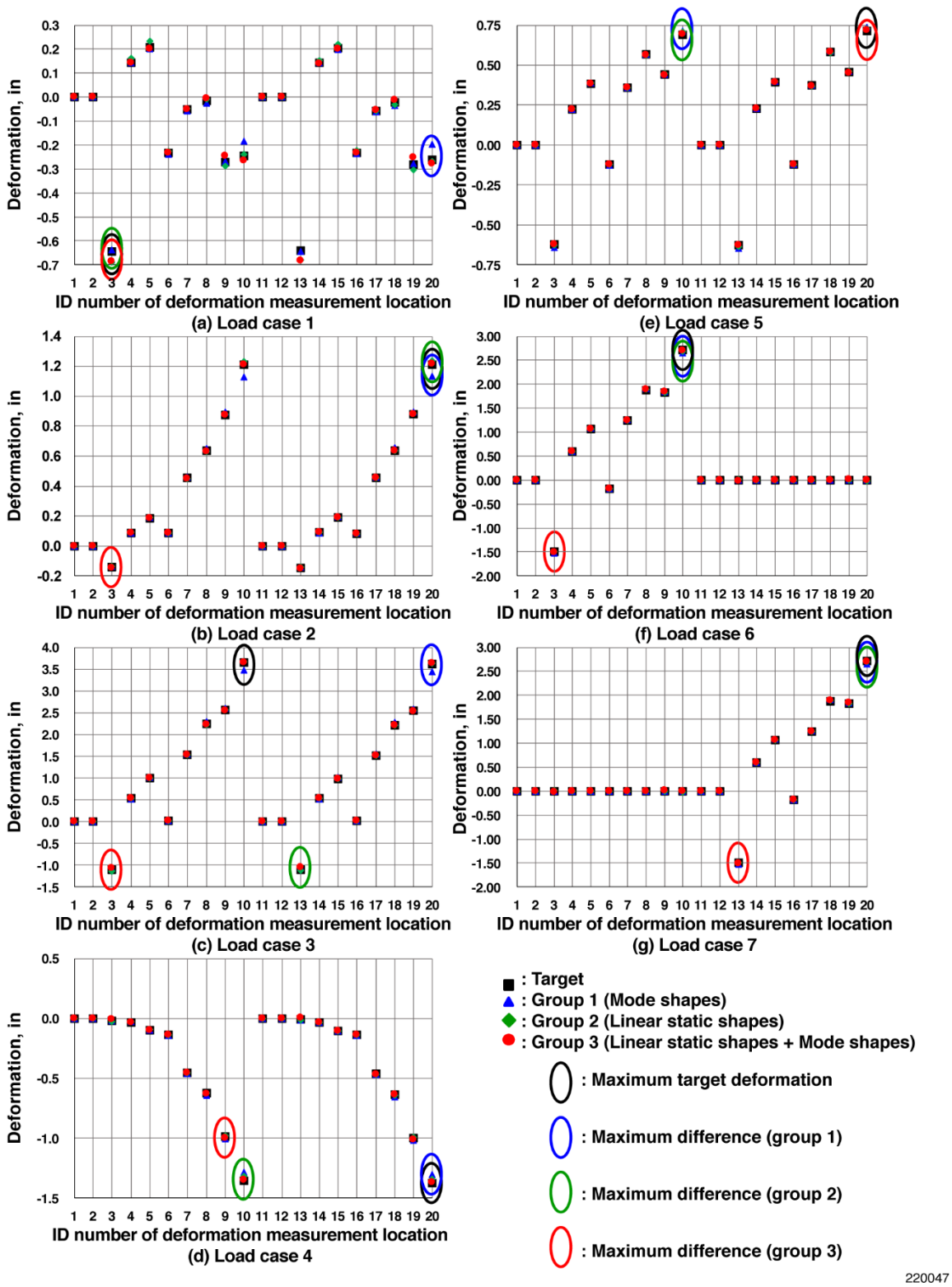

Figure 12. Comparisons of vertical deformations under different basis function groups for seven load cases.

220048

Figure 13. Proof test configuration of the X-59 Quiet Supersonic Technology (QueSST) aircraft (Lockheed Martin, Bethesda, Maryland).

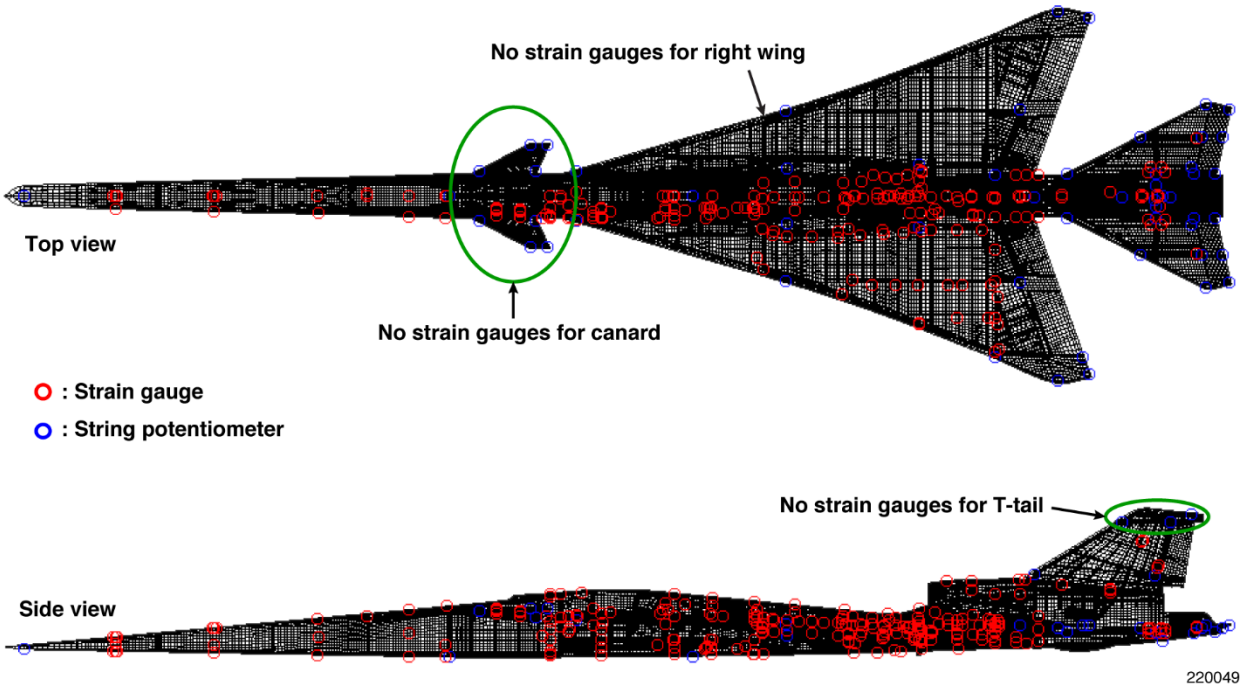

Figure 14. Locations of strain gauges and string potentiometers on the X-59 Quiet Supersonic Technology (QueSST) aircraft (Lockheed Martin, Bethesda, Maryland).

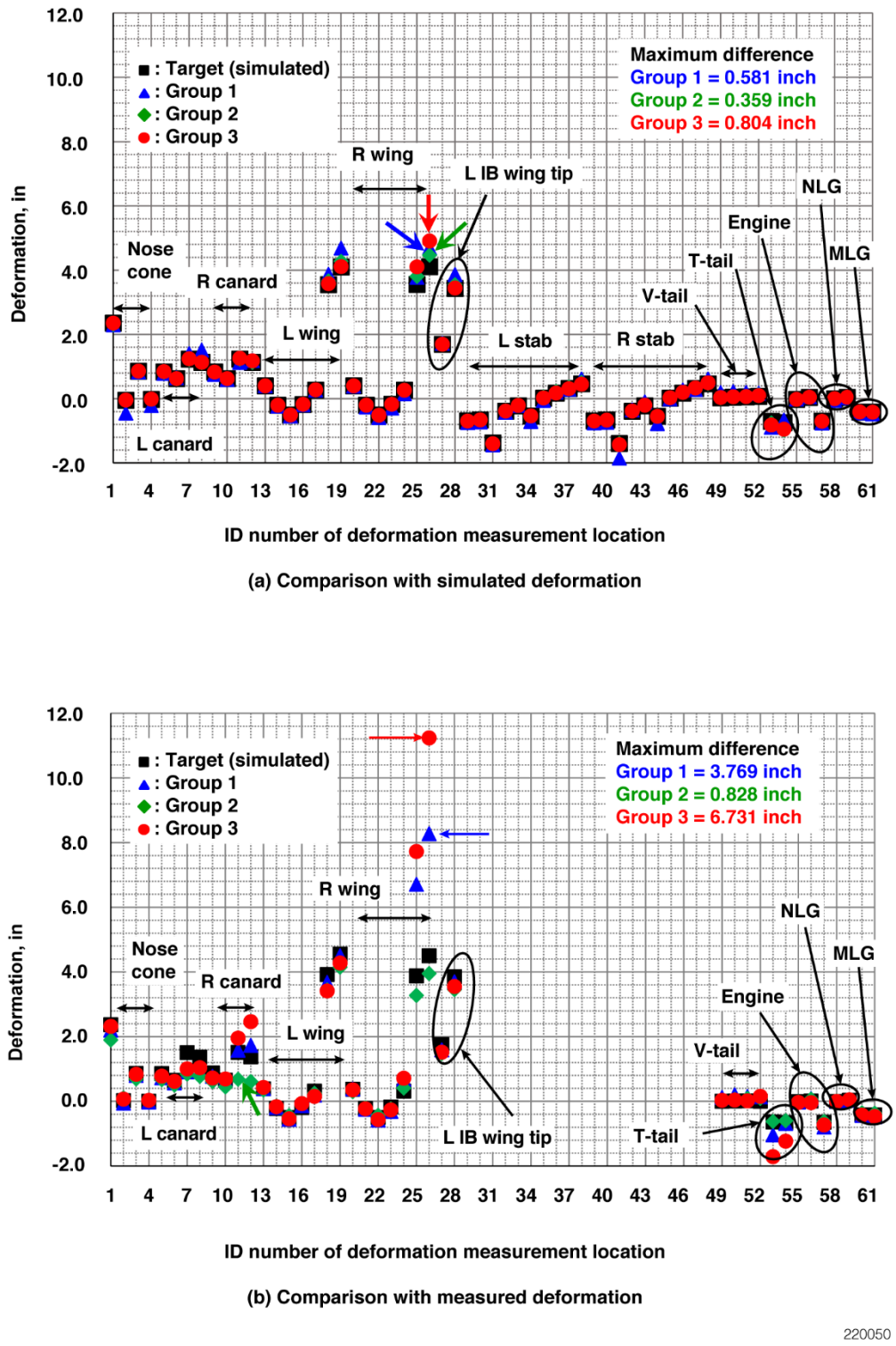

Figure 15. Comparisons of (a) simulated; and (b) measured vertical deformations under different basis function groups for load case 2.

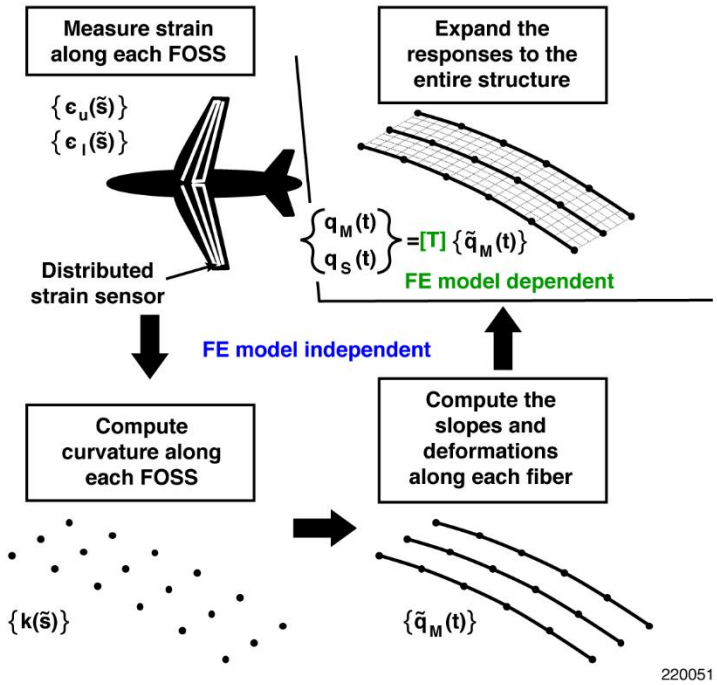

Figure A-1. Block diagram of the mathematical background of the two-step theory.

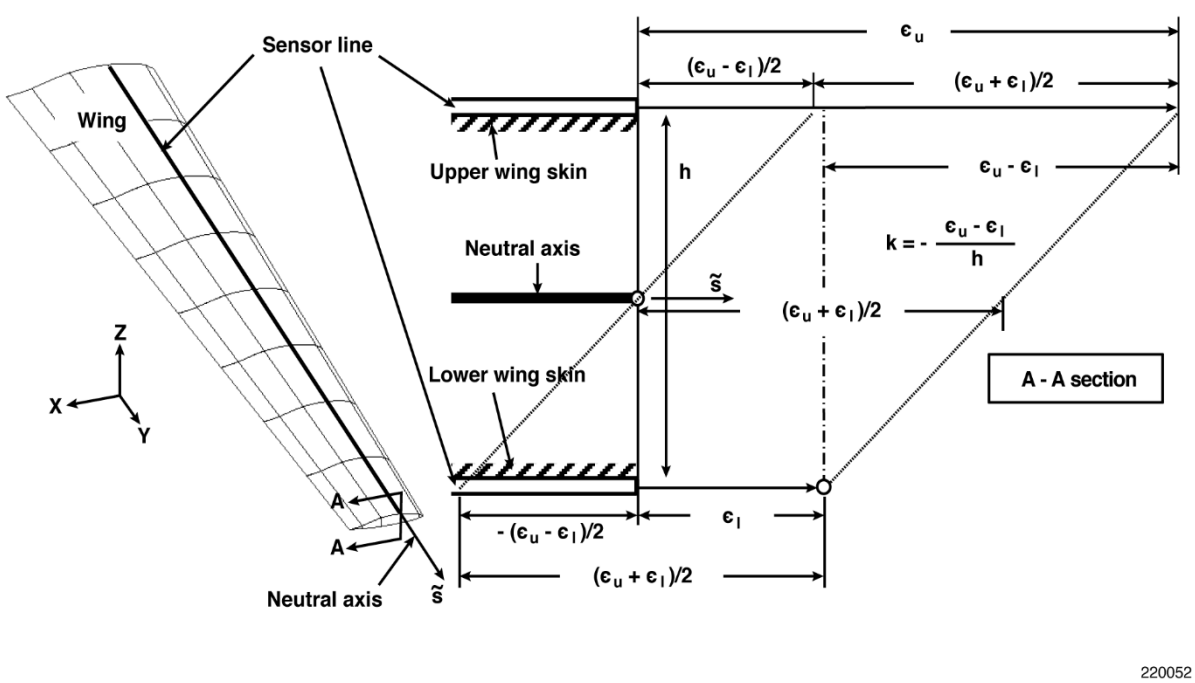

Figure A-2. Definition of curvature, κ, along the neutral axis.

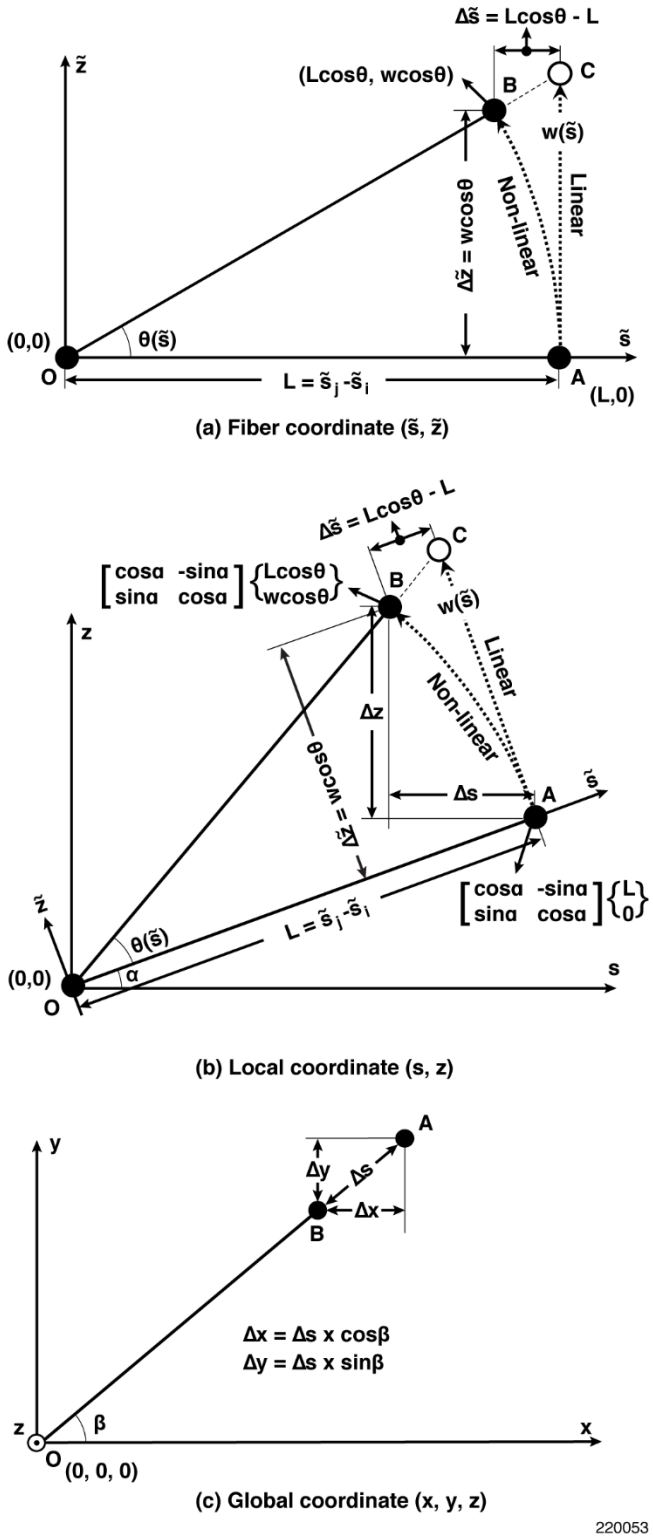

Figure A-3. (a) fiber; (b) local; and (c) global coordinate system for deformation computations.